Dalton Transactions

Accepted Manuscript

ROYAL SOCIETY OF CHEMISTRY

www.rsc.org/dalton

A chemical method for stabilizing a new series of solid solution in $Pr_{1-x}Ce_xScO_3$ ($0.0 \leq x \leq 1.0$) system

Farheen N. Sayed, R. Shukla and A. K. Tyagi*

Chemistry Division, Bhabha Atomic Research Centre, Mumbai - 400085, India

*Corresponding author:

Dr. A. K. Tyagi

Phone: 0091-22-2559 5330

Fax : 0091-22-25505151

E-mail: aktyagi@barc.gov.in

Abstract

A new series of $Pr_{1-x}Ce_xScO_3$ ($0.0 \leq x \leq 1.0$) compounds was synthesized by a two-step synthesis route, involving combustion reaction followed by reduction while heating in low partial pressure of O_2, generated by zirconium sponge that acts as an oxygen getter. For the first time, a perovskite solid solution formation was observed in this series in the entire homogeneity range. These compounds were characterized using XRD, Raman spectroscopy and DRUV-visible spectrophotometer. Rietveld refinement was carried out on the XRD data to determine unit cell parameters, bond lengths, bond angles along with the tilt angles for ScO_6 octahedra. The analyses of the Raman shift were also in agreement with XRD data. All compounds in this series showed decreasing trend in the bandgap from 4.74 to 2.91 eV as a function of increasing Ce^{3+} concentration.

Key words: Perovskite; Gel-combustion; Bandgap

Introduction:

Oxide based perovskites (ABO_3) have been an active research area with its relevance to both fundamental and applied fields. This class of materials illustrate wide range of properties including metal-insulator transitions, anomalous magnetoresistance, dielectric, catalysis and so on.[1-5] Among perovskites, orthorhombic rare-earth scandates ($REScO_3$) have received a growing interest, due to their potential applications in various fields such as single crystal substrates for strain engineered ferroelectrics, multiferroics[6-11] and thin film based high dielectric materials for silicon free MOSFET application.[7,12-17] Primarily, $REScO_3$ materials are excellent high-k dielectrics. In addition, they show good resistance to oxygen diffusion and remain stable in contact with silicon. $PrScO_3$ with pseudocubic lattice parameter slightly larger than that of $BaTiO_3$ has been used for the growth of $BaTiO_3$.[8,18]

All $REScO_3$ form the stable perovskite structure throughout the rare-earth series with small variation in cell parameters, the relatively less stable Ce^{3+} still remains under-explored, due to the inherent difficulty in stabilizing Ce^{3+} compared to its Ce^{4+} counterparts.[19] Till recently there was only one report on synthesis of $CeScO_3$ wherein it was synthesized by arc-melting method.[20] Our group recently reported a two-step synthesis procedure for the stabilization of Ce^{3+} ions in same scandate perovskite structure.[21] The first step involved preparation of homogenized cerium and scandium containing nano-crystalline precursors. In second step the as-prepared nanopowder was chemically reduced in presence of Zr metal in vacuum. To the best of our knowledge there are no reports on synthesis of $Pr_{1-x}Ce_xScO_3$ ($0.0 \leq x \leq 1.0$) system. Taking into consideration the close ionic radii of Pr^{3+} (1.126 Å in 8-fold coordination) and Ce^{3+} (1.143 Å in 8-fold coordination) it was envisaged that there should not be any reason to hinder the formation of $Pr_{1-x}Ce_xScO_3$ series, only problem being stabilization of Ce^{3+}.[22] In view of this, $Pr_{1-x}Ce_xScO_3$ series of solid solutions has been synthesized and explored and results obtained are being discussed in subsequent sections.

Experimental:

$PrScO_3$ was synthesized via solid state route in which first the stoichiometric amounts of Pr_6O_{11} and Sc_2O_3 were thoroughly ground and the resultant mixture was heated at 800 ^oC followed by another heat treatment at 1100 ^oC and 1400 ^oC, for 12 h each in static air, with intermittent grindings. For the preparation of $Pr_{1-x}Ce_xScO_3$ ($0.0 \leq x \leq 1.0$), the glycine-nitrate

combustion reaction was performed with respective metal nitrates in varying oxidant-to-fuel ratios (fuel-deficient ratio 1:1.5 and stoichiometric 1: 3.33) to obtain the nanopowders. The as-prepared powders were calcined at 600 ^{o}C for 1 h in air to remove the volatile carbonaceous impurities. These calcined powders were pelletized, wrapped in a tantalum foil, and vacuum-sealed (10^{-6} mbar pressure) in a quartz tube in the presence of pelletized Zr metal powder (oxygen getter), and heated at 1100 ^{o}C for 12 h. Tantalum foil was taken to avoid the direct contact of sample pellets and Zr metal. In addition, Ta metal also acts as oxygen getter to further facilitate the reduction procedure.

In order to ascertain the oxidation of state of cerium in reduced samples, TGA study was carried out on a representative sample ($Pr_{0.50}Ce_{0.50}ScO_3$) using Thermogravimetry–Differential Thermal Analysis (TG-DTA) instrument (SETARAM SETSYS Evolution) under static air at a scan rate of 10 Kmin^{-1}. All the prepared samples were characterized for their phase identification by X-ray diffraction (XRD) using monochromatized Cu-Kα radiation on RIGAKU XRD unit. Silicon was used as an external standard. XRD data were recorded in range of 10-80^{o} with 0.02^{o} step scan for 2 h. Raman spectroscopic measurements were carried out on a micro/macro-Raman spectrometer (LABRAM-1, France) using the 488-nm line of an Ar^{+} ion laser for excitation with a Peltier-cooled CCD detector in the backscattering geometry. Samples were used in the form of pellets, and the laser line was focused on a flat surface of the sample using an optical microscope (Olympus BX-40, 50x objective lens) connected to the spectrometer. The optical bandgap of $Pr_{1-x}Ce_xScO_3$ ($0.0 \leq x \leq 1.0$) series was measured employing a JASCO Model V-670 DR-UV visible spectrophotometer, with $BaSO_4$ as standard.

Rhodamine B (Rh B) was taken up as the model pollutant to test the efficiency of the lower bandgap material as photocatalyst. For the photocatalytic experiments, a 100 ml batch cylindrical pyrex glass reactor was used. The irradiation source was a 400W medium pressure Hg lamp (SAIC) located inside a quartz tube, situated perpendicularly in the reactor with 170 mW/cm^2 flux for UV based studies and for visible region. The initial concentration of the dye solution was taken to be 10^{-5} M. In a typical experiment, reaction mixture consisted of 50 ml of 10^{-5} M dye solution containing catalyst powder at the concentration of 1 mg/ml. A blank containing 50 ml dye solution without any catalyst was also taken. The dye-catalyst suspension was stirred magnetically for 30 min in dark to attain the adsorption-desorption equilibrium between dye and catalyst. The dye-catalyst suspension and the blank solution were irradiated

with UV light source. Small volumes were withdrawn at regular intervals of time and after separating catalyst from solution by centrifugation, UV-visible spectra were recorded. The extent of Rh B degradation was monitoring by the observing the absorbance peak at 552 nm. These studies were carried out under neutral pH and ambient conditions.

Results and Discussion:

Initially $PrScO_3$ was synthesized by conventional solid state method using three step heating protocol. The XRD pattern of solid state synthesized sample after heating at 1400 ^oC for 12 h is shown in Supplementary Information (**SI-1**). The XRD pattern matches very well with the standard pattern (JCPDS #26-1353) of $PrScO_3$. However, weak reflection peaks other than pure PrScO3 were also observed (indicated in **SI-1**). The color of this solid-state synthesized $PrScO_3$ was brownish grey, indicating the presence of small amount of Pr^{4+} in the sample. Since solid-state method could not yield single phasic compound, gel-combustion method with glycine as fuel was adopted. The oxidant-to-fuel ratio in gel-combustion synthesis governs the exothermicity which in turn decides the stabilization of specific phase along with crystallinity. Two different oxidant-to-fuel ratios i.e. 1:1.5 (40% fuel-deficient ratio) and 1:3.33 (stoichiometric ratio) were selected.

The as-prepared products obtained after fuel-deficient combustion (**SI-2**) were amorphous whereas the products obtained after stoichiometric combustion (**Fig. 1**) were comparatively crystalline. After calcination at 600 ^oC the product of stoichiometric combustion crystallizes completely to phase pure $PrScO_3$ (**Fig. 1**), whereas, fuel-deficient synthesized sample still remains amorphous and only after 1100 ^oC treatment it initiates to crystallize. On high temperature treatment, it was observed that $PrScO_3$ obtained from both oxidant-to-fuel ratios are stable up to the studied temperature i.e. 1400 ^oC. The color of $PrScO_3$ prepared with stoichiometric ratio of glycine on heating at 1100 ^oC was light green, which is the characteristic color of Pr^{3+}, indicating the absence of Pr^{4+} in the sample. Thus, it could be inferred that phase pure $PrScO_3$ can be easily prepared by a facile gel-combustion method using glycine as fuel in stoichiometric ratio.

Based on above optimization of gel-combustion reaction stoichiometric amounts of oxidant and fuel were selected to synthesize $Pr_{1-x}Ce_xScO_3$ ($0.0 \leq x \leq 1.0$) compositions. As mentioned earlier, stabilization of Ce^{3+} in $Pr_{1-x}Ce_xScO_3$ system is unfeasible under ambient

conditions. Hence, the above mentioned two step method was adopted for the synthesis of $Pr_{1-x}Ce_xScO_3$ ($0.0 \leq x \leq 1.0$) compositions.

The XRD patterns of calcined $Pr_{1-x}Ce_xScO_3$ ($0.0 \leq x \leq 1.0$) samples are shown in **Fig. 2**. As was also observed in **Fig. 1**, the calcined products were poorly crystalline. The initial compound (0 mol % Ce^{3+}) (**Fig. 2a)** exhibited peaks corresponding to $PrScO_3$. On substitution of 25 mol% Ce^{3+}, the parent structure $PrScO_3$ is self-accommodating and stabilizing Ce^{3+} at A-site (**Fig. 2b)**. However, as the amount of cerium substitution is increased to 50 mol % (**Fig. 2c)** the structure is unable to stabilize and results in the separate phase formation of Sc substituted CeO_2 along with the Sc_2O_3. For the higher substitution of 75 mol % cerium and the other end member of the series $CeScO_3$, a fluorite type solid solution of Sc substituted CeO_2 were observed. It is also clearly evident that though $PrScO_3$ is obtained as a relatively crystalline product (sharps peaks in XRD pattern), the compositions from other end member side are comparatively amorphous (broad peaks in XRD pattern). Here, broadening of substituted ceria peaks also suggest the nano size of samples. This 'nano size' feature makes cerium containing samples better precursor for a facile and complete reduction of Ce^{4+} to Ce^{3+}. In order to obtain the phase pure products, the calcined samples were reground and pelletized to reduce as mentioned in the experimental section. During this heat treatment in the presence of Zr powder, partial pressure of O_2 in quartz ampoule reduces considerably, which facilitates the reduction of Ce^{4+} to Ce^{3+} and in turn assists the transformation of multi-phasic product into stable perovskite phases. The oxygen partial pressure required to obtain Ce^{3+} (Ce_2O_3) from Ce^{4+} (CeO_2) at 1100 ^oC is ~ 10^{-18} atmospheric pressure.[23] Under above condition an equlibrium between Zr and ZrO_2 is established. The equilibrium oxygen partial pressure under this condition as calculated using standard thermodynamic data is found to be around ~10^{-34} atmosphere.[23] Co-existence of Zr metal and negligibly small amount of ZrO_2 at the end of experiment infers that the equlibrium prevailed during the reaction with ~10^{-34} oxygen partial pressure. The calculated partial pressure is much lower than the pressure required to obtain Ce^{3+} (Ce_2O_3) from Ce^{4+} (CeO_2), and hence stabilization of Ce^{3+} was facilitated in $Pr_{1-x}Ce_xScO_3$ system. Thermogravimetric curve of a representative reduced sample ($Pr_{0.50}Sc_{0.50}ScO_3$) is shown in (SI-3). A weight gain of 1.711% over the temperature range 300-600 ^oC was observed. This is in close agreement with the theoretical weight gain of 1.713%; corresponding to the gain of 0.25 oxygen atom per

$Pr_{0.50}Sc_{0.50}ScO_3$ molecule. This confirms that the reduced sample had cerium in 3+ oxidation state.

The XRD patterns of reduced samples are shown in **SI-4**. Though $PrScO_3$ was stabilized in orthorhombic perovskite structure after the first step of synthesis itself i.e. after gel combustion, to maintain the synthesis conditions identical throughout the series, it was also given the reduction treatment. The 25 mol% Ce^{3+} substituted sample gets further crystallized and matched very well with the parent composition, accompanied with negligible shift in high intensity peak. It was observed that even though the reduction was carried out in presence of twice the amount of Zr, the complete reduction has been not achieved, giving biphasic product and 50 and 75 mol% cerium substituted composition showed presence of mixed phases containing substituted-CeO_2 and cubic Sc_2O_3 (JCPDS #84-1880). Biphasic nature of these samples could be due to barrier layer formation of reduced sample on the interface, hindering the complete reduction. Hence, these compositions were again reduced after regrinding, pelletizing and increasing the amount of Zr metal by twice the previous amount. The XRD patterns of these re-reduced compositions are shown in **SI-5**. It is clearly evident that all the compositions in $Pr_{1-x}Ce_xScO_3$ series have been stabilized in single phasic perovskite structure.

The XRD patterns of these completely reduced compositions were subjected to Rietveld refinement using Fullprof package in the standard setting space group *Pnma* instead of the non standard configuration *Pbam* as used in literature.[24,25] Though, a cyclic lattice transformation can be used to relate the *Pnma* and *Pbnm* settings. The background of the observed diffraction data was fitted using a fifth order polynomial function and the diffraction profile was modeled using pseudo-Voigt profile function. The initial cycles of the Rietveld refinement were carried with the scale, background, and profile parameters along with the unit cell parameters. The temperature coordinates were fixed at zero and the position coordinates were included in the subsequent cycles of refinement. The representative refined XRD patterns of $PrScO_3$, $Pr_{0.5}Ce_{0.5}ScO_3$ and $CeScO_3$ samples are shown in **Fig. 3**. In orthorhombic $REScO_3$, due to smaller size of RE ion, the ScO_6 octahedra tilts/rotates, making the coordination polyhedra for rare-earth 8-fold (4-fold antiprism) rather than 12-fold (cubo-octohedron). This results in transformation of 12 RE-O bonds to 8 short RE-O and 4 long RE-O bonds. In *Pnma* structure the RE and Sc ions are placed at 4c and 4b sites whereas, oxygen atoms are placed at 4c and 8d sites. The refined positional coordinates along with the other refinement parameter are given in Table 1. In accordance with

their increasing ionic radii from Pr^{3+}(1.126Å) to Ce^{3+} (1.143Å) ions in 8-fold coordination,[22] a small but gradual shift in peaks was observed towards lower two theta value i.e. high d-value, confirming the formation of single phasic perovskite solid solutions with increased cell parameters as well as cell volume (Table 1). Tolerance factors for $REScO_3$ throughout the length of RE- series found to be lower than other $REMO_3$ (M = Fe, Cr or Al) based perovskite, suggesting that the $REScO_3$ compositions to be comparatively more distorted.[24] In present study the calculated tolerance factor were found to be 0.8903, 0.8914, 0.8925, 0.8936 and 0.8947 for orthorhombic $PrScO_3$, $Pr_{0.75}Ce_{0.25}ScO_3$, $Pr_{0.50}Ce_{0.50}ScO_3$, $Pr_{0.25}Ce_{0.75}ScO_3$ and $CeScO_3$, respectively. Here, as the tolerance factor increases from $PrScO_3$ to $CeScO_3$ the structure gets more relaxed, in accordance with their ionic radii in 8-fold coordination.

The detailed analysis of refined structural parameters of the $PrScO_3$ shows a close agreement with the values reported earlier.[26] The bond lengths and bond angles obtained after Rietveld refinement of XRD pattern are given in Table 2. In the $PrScO_3$ structure, the Sc atoms form nearly regular octahedra with two O1 and four O2 atoms. The four Sc–O2 (axial) bond lenths are 2.09 Å. The typical apical Sc–O1 bond lengths are 2.11 Å. The ScO_6 octahedral unit of orthorhombic $CeScO_3$ consisted of two longer Sc–O2 (axial) bonds (2.11 Å), two shorter Sc–O2 (axial) bonds (2.10 Å) and two Sc–O1 apical bonds (2.13 Å). These observed bond lengths suggest a negligibly small variation in the local surroundings of the Sc as function of Ce^{3+} content. The intermediate compositions however do not show linear behavior in bond length, plausibly due to the difference in extent of ionicty. The RE-O bonds also showed the same behavior. It is worth mentioning here that the significant variation in both the RE–O bond lengths is also related to the ScO_6 octahedral tilting. In orthorhombic *Pnma* lattice this octahedral tilt is associated with distortions. The distortion parameters in the perovskite lattice can be related to the unit cell strain as well as inter-atomic distances in the octahedral unit. The orthorhombic (*Pnma*) structure of $REScO_3$ can be explained by two direction dependent tilts, namely θ about $(110)_p$ axis and φ about $(001)_p$ axis, where the subscript p represent the primitive (Z¼1) *Pm3m* cubic structure. Also, these two tilts can be represented by a single tilt ϕ about $(111)_p$. Here, the tilt angles θ and φ can be obtained directly either from the unit cell parameters or Sc–O–Sc bond angles or shift of the anions from the ideal positions. In present case the tilt angles were calculated from the observed Sc–O–Sc bond angles according to the methods reported in literature.[27-28] The tilt angles θ, φ and ϕ for ambient temperature orthorhombic

$CeScO_3$ are 18.3°, 8.7°, and 20.2°, respectively. The representative tilt angle ϕ about $(111)_p$ axis for $PrScO_3$, $Pr_{0.75}Ce_{0.25}ScO_3$, $Pr_{0.5}Ce_{0.5}ScO_3$, $Pr_{0.25}Ce_{0.75}ScO_3$ and $CeScO_3$ was 19.9°, 20.6°, 19.8°, 19.3° and 20.2°, respectively. Thus, it was inferred that with varying composition at A-site, the tilt angle for ScO_6 polyhedra did not show much variation.

Raman spectroscopy is more sensitive towards modes involving anions gives the clear insight, compared to average information obtained from XRD data. Orthorhombic $REScO_3$ structure with four Z (formula units per unit cell) obtained by an anti-phase tilt of the adjacent ScO_6 octahedra ($a^-b^+a^-$) in Glazer's notation with respect to the ideal cubic *Pm-3m* perovskite structure give rise to 24 Raman active modes: $7A_g+ 5B_{1g}+ 7B_{2g}+ 5B_{3g}$.[29-30] These 24 modes are predicted, however all of them have been never observed for these systems. Raman spectra obtained for the $Pr_{1-x}Ce_xScO_3$ ($0.0 \leq x \leq 1.0$) compositions are shown in **Fig. 4**. These modes can be seen as one set of modes below 200 cm^{-1}, which change marginally in wavenumber as a function of average ionic radii of RE^{3+}. For comparing different materials of the same symmetry, it is useful to invoke the approximation of the harmonic oscillator which allows evaluating the effect of changing ionic radii and atomic masses in conjunction. The heavier atoms vibrate at lower frequencies, thus the modes of the first group below 200 cm^{-1} are expected to be dominated by vibrations involving the heavier RE atom. Among the lower frequency modes, 6 modes namely $A_g(2)$, $B_{1g}(2)$, $B_{2g}(1)$ and $B_{3g}(1)$ are assigned to the A site cation translation. In present case the A-site cations; Pr^{3+} and Ce^{3+} have a very small difference in ionic radius as well as mass, hence feeble changes are expected in lower frequency region (**Fig. 5**). The peak at 121 cm^{-1} of B_{2g} mode for $PrScO_3$ shifts very little towards relatively higher wavenumber, however the intensity also decreases and in the other end member composition $CeScO_3$, this peak almost diminishes. The other modes at higher frequency 280, 416 and 472 cm^{-1} for the end member do not show any shift. However, in the intermediate compositions ($Pr_{0.75}Ce_{0.25}ScO_3$, $Pr_{0.5}Ce_{0.5}ScO_3$ and $Pr_{0.25}Ce_{0.75}ScO_3$) the blue shifts are observed. Here, it is worth mentioning that these frequency modes are independent of the change in unit cell parameters which showed small but systematic increasing trend. The distortion observed for the substituted compositions can thus be directly influenced from the Sc-O1-Sc bond angle rather than Sc-O2-Sc bond angle. Along with these high frequency modes the same trend is also observed for the low frequency mode at 144 cm^{-1}, Hence, the evolution of all these modes is a combined effect of average ionic radii as well

as atomic masses. From the Raman data it could be inferred that there is not much significant change in the local environment of the sample.

The absorption spectra of $Pr_{1-x}Ce_xScO_3$ ($0.0 \leq x \leq 1.0$) series are recorded (**Fig. 6a**) showing that the samples have strong absorption in UV range. Tauc Mott plot is used to calculate the bandgap of these materials. The following Tauc formula depicting the relationship between absorption coefficient and incident photon energy was used:

$$ahv = A(hv - Eg)^n$$

where, α is absorption coefficient, A is constant and n can be 2 (direct transition) or 0.5 (indirect transition). The indirect bandgap values are calculated and presented in **Fig. 6b**. The parent compound $PrScO_3$ was found to have wide bandgap of 4.74 eV which goes on decreasing upto 2.91 eV ($CeScO_3$) with increasing Ce^{3+} contents. However, the present solid solution does not show the linear variation in bandgap values, which is due to the non-ideal nature of these solid solutions.

As a representative of this series, the end member $CeScO_3$ which showed the near visible light absorption was subjected to photocatalytic studies. The initial studies were performed with the 50 mg of catalyst ($CeScO_3$) and 10^{-5} M Rh B dye solution with respect to a blank solution containing only dye. The kinetic studies in presence of UV light irradiation suggested that the catalyst is UV light active and degraded the ~80% of the dye in 10 h (**Fig. 7**). Under the same conditions blank solution was irradiated and found to have negligible degradation which can be attributed to the self-sensitization of the dye in absence of any catalyst. The $t_{1/2}$ value of this degradtion kinetic was calculated and found to be 5 h. The temporal studies reflected very small shift in the absorption peak. Hence, indicating the degradation via both the direct degradation and formation of another resonance structure. In the present series the bandgap values increases with the increasing Pr^{3+} substitution and also the samples are not in nano-regime after high temperature treatment. The catalytic activity can be improved with decreasing the synthesis temperature.

Conclusion

$PrScO_3$ was synthesized by both conventional solid state method and gel-combustion process. The gel combustion method in stoichiometric ratio yielded phase pure $PrScO_3$ comparatively at lower temperature. The solid solutions of $Pr_{1-x}Ce_xScO_3$ ($0.0 \leq x \leq 1.0$) were

prepared via two-step gel-combustion-reduction method that helped to reduce Ce^{4+} to Ce^{3+} thereby completely stabilizing the series in distorted perovskite orthorhombic structure. The prepared samples were characterized by XRD to determine unit cell parameters, bond lengths, bond angles along with the tilt angles for ScO_6 octahedra. The structural data were further corroborated with Raman spectroscopy, focusing on the increased distortion. DRUV-VIS studies revealed varying bandgap from 4.74 to 2.91 eV in $Pr_{1-x}Ce_xScO_3$ system. The potential of the representative composition $CeScO_3$ showed UV light activity for degradation of Rh B.

Acknowledgement

The Department of Atomic Energy's Science Research Council (DAE-SRC) is acknowledged for supporting this work, vide sanction number no. 2010/21/9-BRNS/2025 dated 7-12-2010.

References

1 V. Grover, R. Shukla, D. Jain, S. K. Deshpande, A. Arya, C. G. S. Pillai and A. K. Tyagi, *Chem Mater*., 2012**, 24**, 2186-2196.

2 K. I. Kobayashi, T. Kimura, H. Sawada, K. Terakura and Y. Tokura, *Nature*, 1998, **395**, 677-680.

3 M. Dawber, K. M. Rabe and J. F. Scott, *Rev. Mod. Phys*., 2005, **77**, 1083-1130.

4 Y. Tokura, *Physica B: Condens. Matter*., 1997**, 237–238**, 1-5.

5 J. Zhu, H. Li, L. Zhong, P. Xiao, X. Xu, X. Yang, Z. Zhao and J. Li, *ACS Catal*., 2014, **4**, 2917-2940.

6 J. Kreisel, B. Noheda and B. Dkhil, *Phase Transitions*, 2009**, 82**, 633-661.

7 J. H. Haeni, P. Irwin, W. Chang, R. Uecker, P. Reiche, Y. L. Li, S. Choudhury, W. Tian, M. E. Hawley, B. Craigo, A. K. Tagantsev, X. Q. Pan, S. K. Streiffer, L. Q. Chen, S. W. Kirchoefer, , J. Levy and D. G. Schlom, *Nature*, 2004, **430**, 758-761.

8 K. J. Choi, M. Biegalski, Y. L. Li, A. Sharan, J. Schubert, R. Uecker, P. Reiche, Y. B. Chen, X. Q. Pan, V. Gopalan, L. Q. Chen, D. G. Schlom and C. B. Eom, *Science*, 2004**, 306**, 1005-1009.

9 A. Vasudevarao, A. Kumar, L. Tian, J. H. Haeni, Y. L. Li, C. J. Eklund, Q. X. Jia, R. Uecker, P. Reiche, K. M. Rabe, L. Q. Chen, D. G. Schlom and V. Gopalan, *Phys. Rev. Lett*., 2006, **97**, 257602.

10 G. Catalan, A. Janssens, G. Rispens, S. Csiszar, O. Seeck, G. Rijnders, D. H. A. Blank and B. Noheda, *Phys. Rev. Lett*., 2006**, 96**, 127602.

11 R. Wördenweber, E. H. R. Kutzner and J. Schubert, *J. App. Phys*., 2007**,102**, 044119.

12 T. Heeg, M. Wagner, J. Schubert, C. Buchal, M. Boese, M. Luysberg, E. Cicerrella and J. L. Freeouf, *Microelectron. Eng*., 2005, **80**, 150-153.

13 S. G. Lim, S. Kriventsov, T. N. Jackson, J. H. Haeni, D. G. Schlom, A. M. Balbashov, J. L. Freeouf and G. Lucovsky, *J. App. Phys*., 2002, **91**, 4500.

14 G. Lucovsky, Y. Zhang, J. L. Whitten, D. G. Schlom and J. L. Freeouf, *Microelectron. Eng*., 2004, **72**, 288-293.

15 G. Lucovsky, J. G. Hong, C. C. Fulton, Y. Zou, R. J. Nemanich, H. Ade and D. G. S. Schlom, *Phys. Status Solidi B*, 2004, **241**, 2221-2235.

16 P. Delugas, V. Fiorentini, A. Filippetti and G. Pourtois, *Phys. Rev. B*, 2007, **75**, 115126.

17 H. M. Christen, Jr. G. E. Jellison, I. Ohkubo, S. Huang, M. E. Reeves, E. Cicerrella, J. L. Freeouf, Y. Jia and D. G. Schlom, *App. Phys. Lett*., 2006, **88**, 262906.

18 J. Schubert, O. Trithaveesak, A. Petraru, C. L. Jia, R. Uecker, P. Reiche and D. G. Schlom, *Appl. Phys. Lett*., 2003, **82**, 3460.

19 R. Shukla, J. Manjanna, A. K. Bera, S. M. Yusuf and A. K. Tyagi, *Inorg. Chem*., 2009**, 48**, 11691-11696.

20 J. E. Greedan and K. Seto, *Mat. Res. Bull*., 1981, **16**, 1479-1485,

21 R. Shukla, A. Arya and A. K. Tyagi, *Inorg. Chem*., 2009, **49**, 1152-1157.

22 R. D. Shannon, *Acta Cryst. B*, 1976, **A32**, 751-767.

23 G. V. Belov, B. G. Trusev, ASTD-Computer aided Reference Book in Thermodynamical, Thermochemical & Thermophysical properties of species, Version 2.0, Moscow, (1983-1995)

24 P. Ruslan and R. H. M. Liferovich, *J. Solid State Chem*., 2004, **177**, 2188-2197.

25 T. Roisnel and J. R. Caravajal, Fullprof suite, Software for Rietveld refinement 2008.

26 T. M. Gesing, R. Uecker and J. Chr. Buhl, *Z. Kristallogr. NCS*, 2009, **224**, 365-366.

27 Y. Zhao, D. J. Weidner, J. B. Parise and D. E. Cox, *Phys. Earth Planet. Mater*., 1993, **76**, 17-34.

28 P. Dhak, P. Pramanik, S. Bhattacharya, A. Roy, S. N. Achary and A. K. Tyagi, *Phys. Status Solidi B*, 2011, **248**, 1884–1893.

29 A. M. Glazer, *Acta Cryst. B*, 1972, **28**, 3384-3392.

30 M. N. Iliev, M. V. Abrashev, H. G. Lee, V. N. Popov, Y. Y. Sun, C. Thomsen, R. L. Meng and C. W. Chu, *Phys. Rev. B; Condens. Matter*., 1998, **57**, 2872.

Table Captions:

Table 1: Typical Rietveld refined cell parameters for $Pr_{1-x}Ce_xScO_3$ ($0.0 \leq x \leq 1.0$)

Table 2: The bond lengths and bond angles obtained from Rietveld refinement of XRD pattern

Figure Captions:

Fig. 1: XRD patterns stoichiometric combustion synthesized $PrScO_3$ (a) as prepared (b) 600 ^oC heated (c) 1100 ^oC heated and (d) 1400 ^oC heated

Fig. 2: XRD patterns of stoichiometric combustion synthesized $Pr_{1-x}Ce_xScO_3$ ($0.0 \leq x \leq 1.0$) calcined at 600 ^oC (a) $PrScO_3$ (b) $Pr_{0.75}Ce_{0.25}ScO_3$ (c) $Pr_{0.5}Ce_{0.5}ScO_3$ (d) $Pr_{0.25}Ce_{0.75}ScO_3$ and (e) $CeScO_3$

Fig. 3: Rietveld refined XRD pattern of (i) $PrScO_3$, (ii) $Pr_{0.5}Ce_{0.5}ScO_3$ and (iii) $CeScO_3$ obtained by heating treatment at 1100 ^oC

Fig. 4: Raman spectra of $Pr_{1-x}Ce_xScO_3$ ($0.0 \leq x \leq 1.0$) (a) $PrScO_3$ (b) $Pr_{0.75}Ce_{0.25}ScO_3$ (c) $Pr_{0.5}Ce_{0.5}ScO_3$ (d) $Pr_{0.25}Ce_{0.75}ScO_3$ and (e) $CeScO_3$

Fig. 5: Selected modes of vibration as a function of Ce^{3+} concentration in $Pr_{1-x}Ce_xScO_3$ ($0.0 \leq x \leq 1.0$)

Fig. 6: (a) Absorption spectra and (b) Tauc plots with bandgap values of $Pr_{1-x}Ce_xScO_3$ ($0.0 \leq x \leq 1.0$)

Fig. 7: Temporal Absorption spectra of Rh B with $CeScO_3$ as catalyst under UV light irradiation (inset shows the negligible temporal change in blank dye solution under same condition)

Supplementary Information:

SI-1: XRD patterns of $PrScO_3$ sample synthesized by solid state route after heating at 1400 ^oC for 12 h

SI-2: XRD patterns of fuel deficient combustion synthesized $PrScO_3$ (a) as prepared (b) 600 ^oC heated (c) 1100 ^oC heated and (d) 1400 ^oC heated

SI-3: Thermogravimetric curve for $Pr_{0.50}Ce_{0.50}ScO_3$

SI-4: XRD patterns of stoichiometric combustion synthesized $Pr_{1-x}Ce_xScO_3$ ($0.0 \leq x \leq 1.0$) after first reduction (a) $PrScO_3$ (b) $Pr_{0.75}Ce_{0.25}ScO_3$ (c) $Pr_{0.5}Ce_{0.5}ScO_3$ (d) $Pr_{0.25}Ce_{0.75}ScO_3$ and (e) $CeScO_3$

SI-5: XRD patterns of stoichiometric combustion synthesized $Pr_{1-x}Ce_xScO_3$ ($0.0 \leq x \leq 1.0$) after second reduction (a) $PrScO_3$ (b) $Pr_{0.75}Ce_{0.25}ScO_3$ (c) $Pr_{0.5}Ce_{0.5}ScO_3$ (d) $Pr_{0.25}Ce_{0.75}ScO_3$ and (e) $CeScO_3$

Table 1: Typical Rietveld refined cell parameters for $Pr_{1-x}Ce_xScO_3$ ($0.0 \leq x \leq 1.0$)

Mol. formula	**$PrScO_3$**	**$Pr_{0.75}Ce_{0.25}ScO_3$**	**$Pr_{0.50}Ce_{0.50}ScO_3$**	**$Pr_{0.25}Ce_{0.75}ScO_3$**	**$CeScO_3$**
Mol. Wt.	233.86	233.66	233.46	233.27	233.07
Sp. Grp.	*Pnma* (62)	*Pnma* (62)	*Pnma* (62)	*Pnma* (62)	*Pnma* (62)
Z	4	4	4	4	4
Unit cell Parameter (Å)					
a	5.7740 (2)	5.7772 (2)	5.7781 (2)	5.7800 (2)	5.7761 (3)
b	8.0236 (3)	8.0339 (3)	8.0395 (3)	8.0457 (2)	8.0478 (4)
c	5.6085 (2)	5.6215 (2)	5.6279 (2)	5.6370 (2)	5.6464 (3)
***Volume*(Å^3)**	259.93 (2)	260.75 (1)	261.47 (2)	262.14 (1)	262.48 (2)
Ce^{3+}/Pr^{3+}					
x	0.0502 (3)	0.0491 (3)	0.0485 (3)	0.0473 (3)	0.0441 (3)
y	0.2500	0.2500	0.2500	0.2500	0.2500
z	-0.0110 (5)	-0.0093 (5)	-0.0097 (5)	-0.0093 (5)	-0.0084 (6)
Sc^{3+}					
x	0.0000	0.00000	0.00000	0.00000	0.00000
y	0.0000	0.00000	0.00000	0.00000	0.00000
z	0.5000	0.50000	0.50000	0.50000	0.50000
O^{2-} (1)					
x	0.4671 (26)	0.46510 (28)	0.4671 (30)	0.4704 (29)	0.4582 (29)
y	0.2500	0.25000	0.2500	0.2500	0.2500
z	0.1005 (29)	0.11036 (31)	0.0962 (32)	0.1023 (31)	0.1103 (33)
O^{2-} (2)					
x	0.3001 (21)	0.30283 (22)	0.3005 (24)	0.2988 (22)	0.3004 (23)
y	0.0490 (16)	0.05081 (18)	0.0533 (18)	0.0508 (18)	0.0518 (19)
z	0.6944 (20)	0.69569 (22)	0.7017 (25)	0.7000 (23)	0.7045 (25)
No of free parameters	18	18	18	18	17
Profile	pseudo-Voigt				
Goodness-of-fit (χ^2)	1.79	1.62	1.76	1.91	1.56
R_p, R_{wp},R_{exp}	12.9, 7.8, 13.3	13.2,18.2,14.3	13.1,17.4, 13.1	14.2,19.4, 14.0	11.9, 16.1, 12.8

Table 2: The bond lengths and bond angles obtained from Rietveld refinement of XRD pattern.

	$PrScO_3$	$Pr_{0.75}Ce_{0.25}ScO_3$	$Pr_{0.5}Ce_{0.5}ScO_3$	$Pr_{0.25}Ce_{0.75}ScO_3$	$CeScO_3$
Bond lengths (ScO_6) Å					
Sc-O1x **2**	2.09 (1)	2.12 (1)	2.09 (1)	2.10 (1)	2.11 (1)
Sc-O2x **2**	2.09 (1)	2.10 (1)	2.08 (1)	2.10 (1)	2.10 (1)
Sc-O2x **2**	2.11(1)	2.10 (2)	2.12 (2)	2.10 (2)	2.13 (2)
Bond lengths (REO_8)Å					
RE-O1	2.48 (2)	2.51(2)	2.49 (1)	2.52 (1)	2.50 (2)
RE-O1	2.36 (2)	2.27 (2)	2.37 (2)	2.34 (2)	2.31(2)
RE-O2x **2**	2.71 (1)	2.76(1)	2.70 (1)	2.71(1)	2.71 (1)
RE-O2x **2**	2.39 (1)	2.40 (1)	2.39 (1)	2.40 (1)	2.39 (1)
RE-O2x **2**	2.81(1)	2.77(1)	2.85 (1)	2.83(1)	2.86 (1)
Bond angles (^{o})					
Sc-O1-Sc	146.8 (2)	144.1 (2)	148.1 (2)	146.7 (2)	143.3 (2)
Sc-O2-Sc	147.8 (6)	147.2 (4)	147.8 (4)	148.4 (4)	148.7 (4)

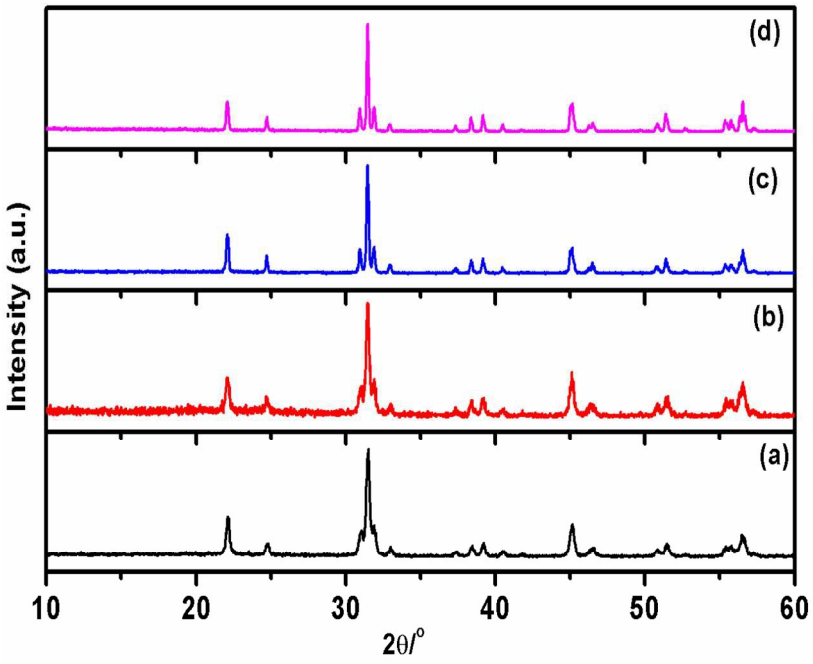

Fig. 1: XRD patterns stoichiometric combustion synthesized $PrScO_3$ (a) as prepared (b) 600 ^oC heated (c) 1100 ^oC heated and (d) 1400 ^oC heated

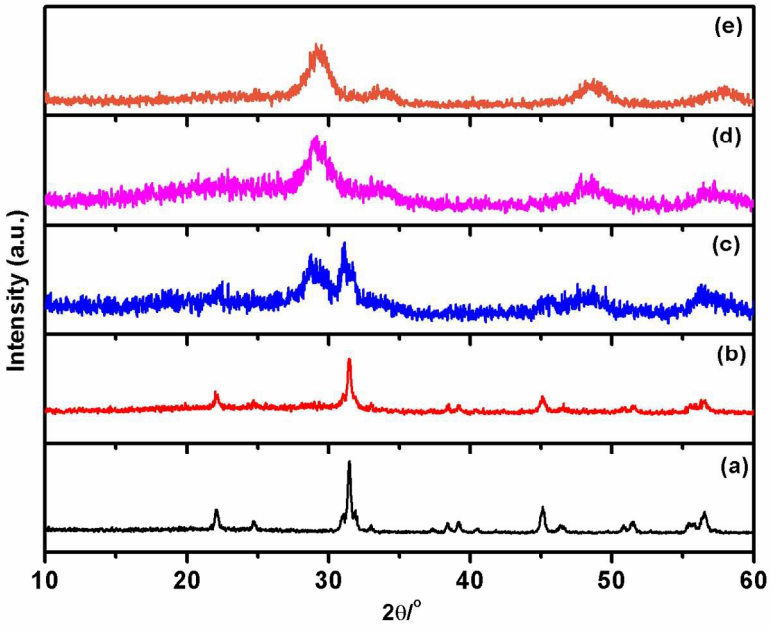

Fig. 2: XRD patterns of stoichiometric combustion synthesized $Pr_{1-x}Ce_xScO_3$ ($0.0 \leq x \leq 1.0$) calcined at 600 ^oC (a) $PrScO_3$ (b) $Pr_{0.75}Ce_{0.25}ScO_3$ (c) $Pr_{0.5}Ce_{0.5}ScO_3$ (d) $Pr_{0.25}Ce_{0.75}ScO_3$ and (e) $CeScO_3$

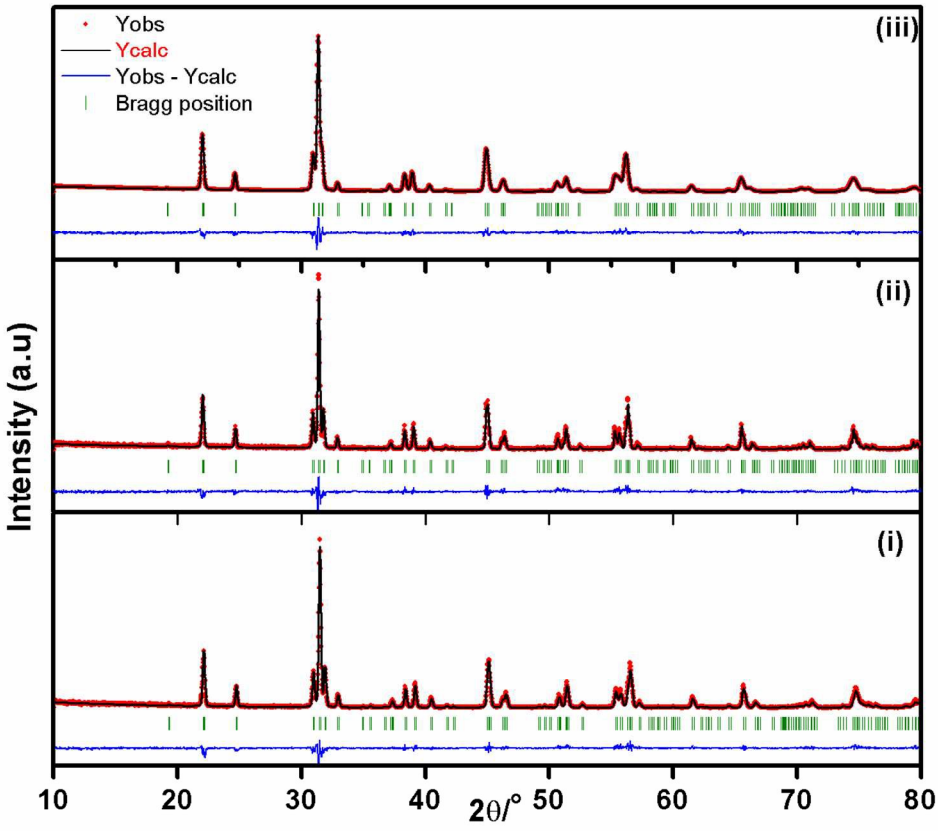

Fig. 3: Rietveld refined XRD pattern of (i) $PrScO_3$, (ii) $Pr_{0.5}Ce_{0.5}ScO_3$ and (iii) $CeScO_3$ obtained by heating treatment at 1100 ^oC

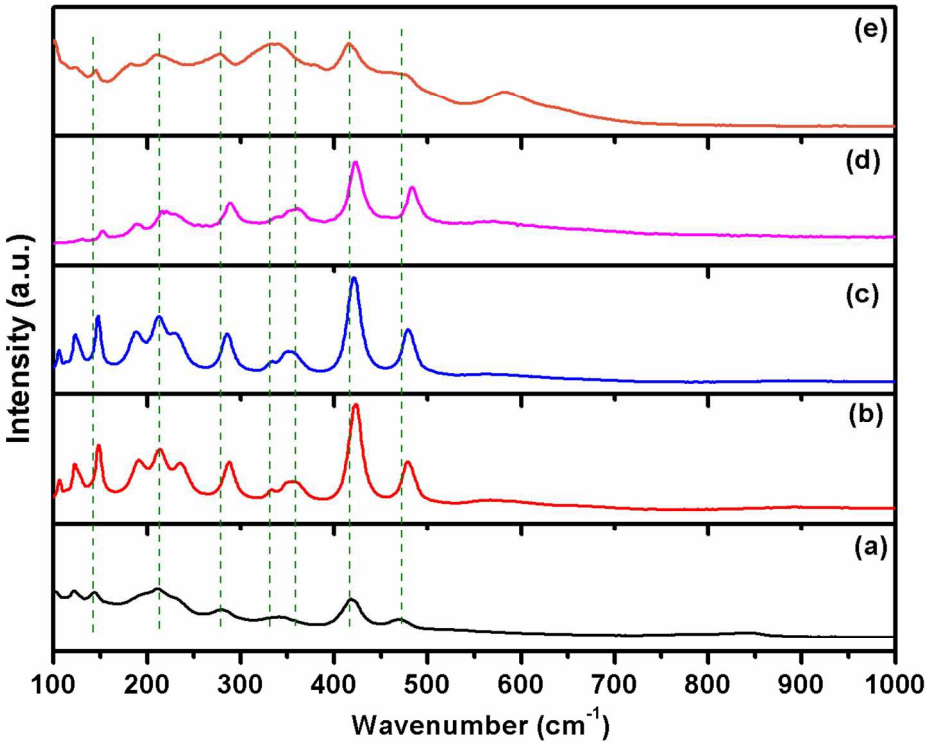

Fig. 4: Raman spectra of $Pr_{1-x}Ce_xScO_3$ ($0.0 \leq x \leq 1.0$) (a) $PrScO_3$ (b) $Pr_{0.75}Ce_{0.25}ScO_3$ (c) $Pr_{0.5}Ce_{0.5}ScO_3$ (d) $Pr_{0.25}Ce_{0.75}ScO_3$ and (e) $CeScO_3$

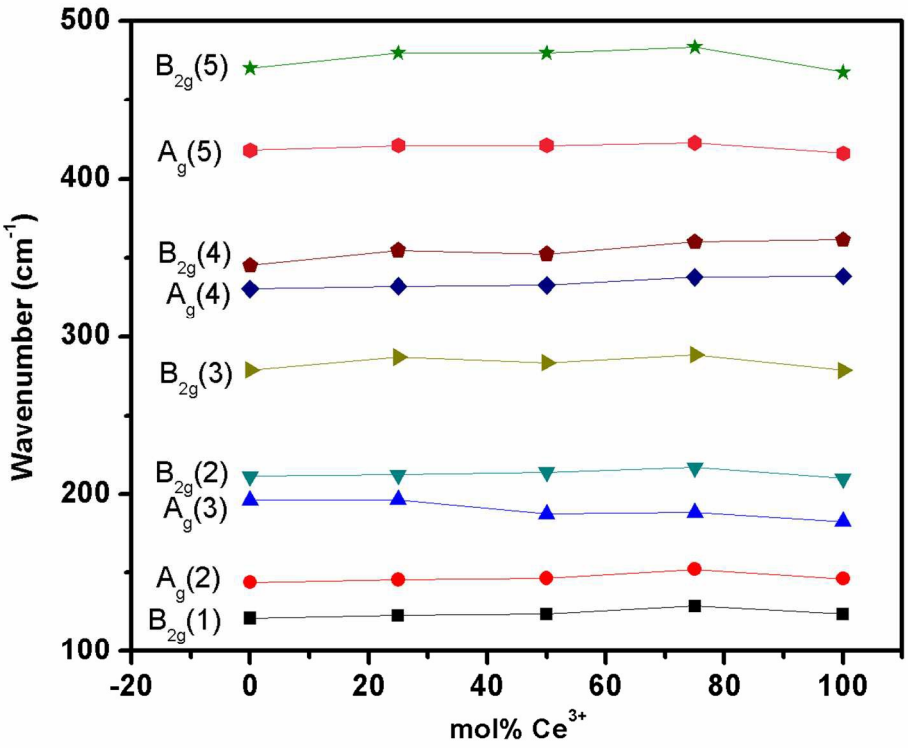

Fig. 5: Selected modes of vibration as a function of Ce^{3+} concentration in $Pr_{1-x}Ce_xScO_3$ ($0.0 \leq x \leq 1.0$)

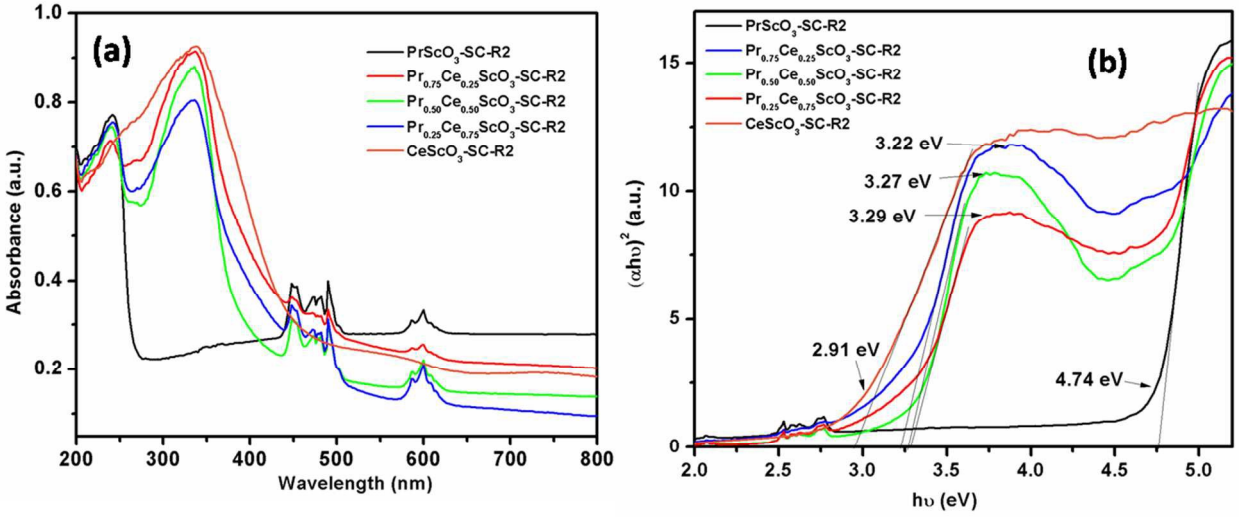

Fig. 6: (a) Absorption spectra and (b) Tauc plots with bandgap values of $Pr_{1-x}Ce_xScO_3$ ($0.0 \leq x \leq 1.0$)

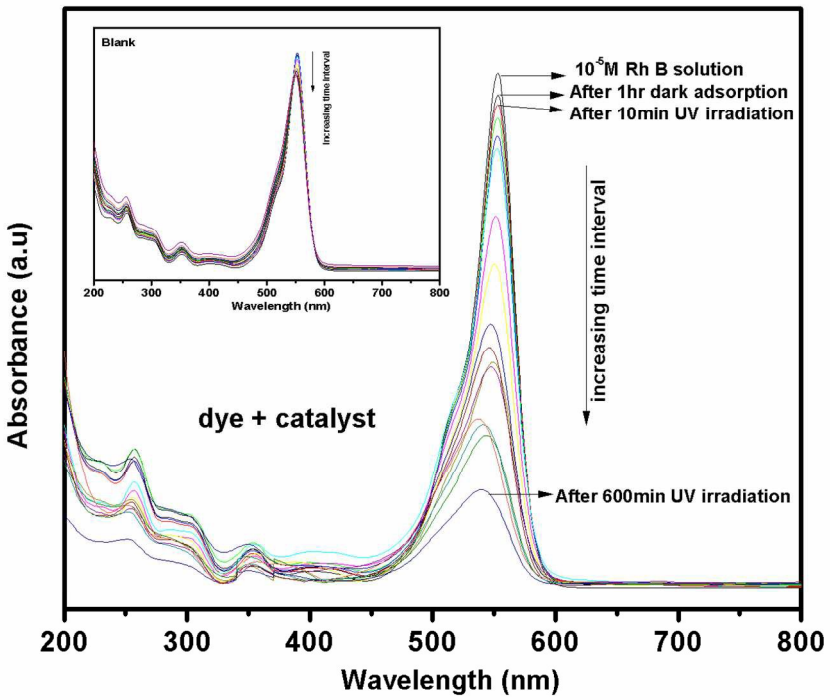

Fig. 7: Temporal Absorption spectra of Rh B with $CeScO_3$ as catalyst under UV light irradiation (inset shows the negligible temporal change in blank dye solution under same condition)

"Table of content"

Structural stabilization of new series of perovskite $Pr_{1-x}Ce_xScO_3$ ($0.0 \leq x \leq 1.0$) system with tunability of bandgap